HHS Public Access

Author manuscript

ACS Catal. Author manuscript; available in PMC 2018 July 07.

Published in final edited form as:

ACS Catal. 2017 July 7; 7(7): 4623–4636. doi:10.1021/acscatal.7b00901.

Catalytic Mechanisms for Cofactor-Free Oxidase-Catalyzed Reactions: Reaction Pathways of Uricase-Catalyzed Oxidation and Hydration of Uric Acid

Donghui Wei[1,2], **Xiaoqin Huang**[2,3], **Yan Qiao**[1,2], **Jingjing Rao**[4], **Lu Wang**[4], **Fei Liao**[4], and **Chang-Guo Zhan**[2,5,*]

[1]College of Chemistry and Molecular Engineering, Zhengzhou University, 100 Science Avenue, Zhengzhou, Henan, 450001, P. R. China

[2]Department of Pharmaceutical Sciences, College of Pharmacy, University of Kentucky, 789 South Limestone Street, Lexington, KY 40536

[3]Center for Theoretical Biological Physics, and Center for Research Computing, Rice University, Houston, TX 77030

[4]Key Laboratory of Medical Laboratory Diagnostics of the Education Ministry, College of Laboratory Medicine, Chongqing Medical University, No.1, Yixueyuan Road, Chongqing 400016, China

[5]Molecular Modeling and Biopharmaceutical Center, College of Pharmacy, University of Kentucky, 789 South Limestone Street, Lexington, KY 40536

Abstract

First-principles quantum mechanical/molecular mechanical (QM/MM)-free energy calculations have been performed to uncover how uricase catalyzes metabolic reactions of uric acid (UA), demonstrating that the entire reaction process of UA in uricase consists of two stages–oxidation followed by hydration. The oxidation consists of four steps: (1) chemical transformation from 8-hydroxyxythine to an anionic radical *via* a proton transfer along with an electron transfer, which is different from the previously proposed electron-transfer mechanism that involves a dianion intermediate (UA^{2-}) during the catalytic reaction process; (2) proton transfer to the O_2^- anion (radical); (3) diradical recombination to form a peroxo intermediate; (4) dissociation of H_2O_2 to generate the dehydrourate. Hydration, for the most favorable pathway, is initiated by the nucleophilic attack of a water molecule on dehydrourate, along with a concerted proton transfer through residue Thr69 in the catalytic site. According to the calculated free energy profile, the hydration is the rate-determining step, and the corresponding free energy barrier of 16.2 kcal/mol

*Corresponding author. zhan@uky.edu.

Notes

The authors declare no competing financial interest.

Supporting Information

Addional figures for the QM/MM-optimized structures associated with other possible reaction pathways and free energy profiles, as well as Cartesian coordinates of the QM atoms of the reaction system in all of the QM/MM-optimized key stationarary points for the possible pathways. A table (Table S1) for the experimental activity data. The Supporting Information is available free of charge on the ACS Publications website: http://pubs.acs.org.

is consistent with that derived from experimental kinetic data, suggesting that the computational insights into the catalytic mechanisms are reasonable. The mechanistic insights not only provide a mechanistic base for future rational design of uricase mutants with improved catalytic activity against uric acid as an improved enzyme therapy, but also are valuable for understanding a variety of other cofactor-free oxidase-catalyzed reactions involving an oxygen molecule.

Graphical Abstract

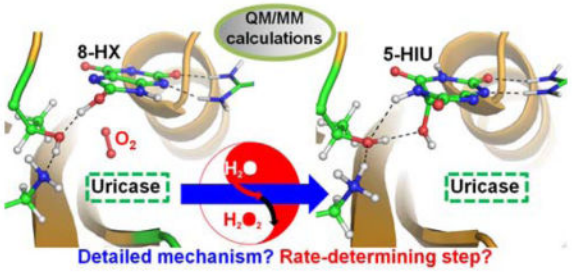

Keywords

Uricase; cofactor-free oxidase; oxidation; QM/MM; catalytic mechanism; uric acid

Introduction

Uric acid (UA) is the product of xanthine oxidase-catalyzed oxidation of xanthine in human body, and is usually maintained at a concentration of 3.6–8.3 mg/dL in blood plasma.[1] Part of UA acts as a physiologically important antioxidant and radical scavenger.[2] Surplus UA is excreted daily through urinary system as there is no natural enzyme in the body of higher primates to catalyze its oxidation. The absence of this specific enzyme, called uricase or uric oxidase, is believed to be a selective advantage and the consequence of genetic mutations and deletions within the coding sequence of the gene.[3] However, elevated serum UA in human body mostly leads to hyperuricemia. Longstanding hyperuricemia certainly results in gouty arthritis and renal stones, which is characterized by the deposition of monosodium UA monohydrate crystals.[4] In the case of tumor lysis syndrome, the UA level is extremely high, resulting in the rapid loss of kidney function.[5] The major hurdles of using an uricase protein as an exogenous enzyme therapy for human exist in the strong immunogenicity of the protein and its very short biological half-life. To overcome these problems for clinical development, uricase was engineered using the monomethoxyl polyethylene glycol (mPEG) to produce the PEGylated uricase to significantly prolong the biological half-life and reduce the immunogenicity.[1,5c,6] Despite the effort to decrease the immunogenicity, a problem which may make the enzyme therapy ineffective, immune responses of humans to the PEGylated uricase are still significant. For example, when treated with a dose of 8 mg PEGylated uricase for every 2 weeks, most of patients with refractory gout could not achieve the intended benefit,[6b] due to the immune responses. It has been well-known that the immune responses of humans (or animals) to a given protein drug are generally dependent on the actual dose of the protein drug used; the higher the dose, the more quickly the humans (or animals) produce antibodies against the drug.[7] Hence, the use of an uricase

mutant with improved catalytic activity against UA would help to decrease the dose required and, thus, decrease the immune responses during the treatment. It is an ideal way to develop an uricase mutant with significantly improved catalytic activity against UA for truly effective treatment of patients suffering from hyperuricemia disorders.[5c,6,8]

In general, for rational design of an enzyme mutant with improved catalytic activity, one first needs to understand the detailed catalytic mechanism, as seen in previous computational enzyme redesign efforts for other therapeutic purposes.[9] So, a detailed mechanistic understanding of how uricase catalyzes the oxidation and hydration of UA could provide an important mechanistic base for the rational design of uricase mutants with improved catalytic efficiency against UA. There have been extensive experimental studies on the kinetic reaction mechanism of uricase by means of spectroscopic characterization, ^{18}O isotope-trapping experiments, stopped-flow kinetic studies, and various enzymatic assays.[10] It has been suggested that the catalytic reaction starts from the binding of O_2 molecule, and proceeded by the release of an intermediate hydroperoxide (H_2O_2).[10d,11] However, these experimental and computational studies failed to identify the molecular species of actual substrate. Recent X-ray and neutron crystal structures of uricase binding with different inhibitors and UA have provided fundamental insights into the possible enzyme-substrate binding mode in the catalytic site of the enzyme.[11h–11k] As revealed in the crystal structure of thermophilic *Bacillus* sp. TB-90[12] bound with inhibitor 8-azaxanthine, extensive electrostatic and hydrogen-bonding interactions with the inhibitor are contributed by highly conserved residues Arg201, Gln250, Asn276, and Gln304 from one subunit, and residues Thr73 and Asp74 from another subunit. The binding site of O_2 has also been determined to be at a site ~3 Å above the inhibitor and formed a hydrogen-bonding network with residues Asn276, Gln304, and Thr73 from the neighboring subunit.[11i,11k] The X-ray structure of *Aspergillus flavus* uricase[11h] in complex with UA and chloride ion (PDB entry of 3L9G with resolution of 1.75 Å) showed that the binding mode of UA with the uricase was very similar as the binding mode of 8-azaxanthine with *Bacillus* sp. TB-90 uricase. The neutron crystal structure of *Aspergillus flavus* uricase with a chloride anion in the binding site of oxygen molecule (PDB entry of 4N9M with resolution of 2.30 Å) revealed that the substrate was bound as 8-hydroxyxanthine (*i.e.* the mono-anion as the enol tautomer).[11g] Another study on *Aspergillus flavus* uricase showed the direct evidence that the peroxide intermediate (C5(S)-(hydro)peroxide) was one of the intermediates for the uricase-catalyzed oxidation of UA.[11f] However, these structural studies[11f–11k] are not enough to reveal the catalytic reaction pathway. It is highly desired for rational uricase redesign and for understanding how a cofactor-free oxidase can accelerate the oxidation reaction to uncover the detailed catalytic mechanism including the catalytic reaction pathways and the corresponding free energy profiles.

Based on available knowledge in literature,[10a–10c,11a,11b,11e,11g,13] the uricase-catalyzed reaction may consist of two stages as shown in Scheme 1. The first stage is for O_2 reduction and H_2O_2 release, starting from the 8-hydroxyxanthine (8-HX),[11g] and to the intermediate dehydrourate. According to Scheme 1, the first reaction step should involve a proton transfer from 8-HX and, thus, UA dianion (UA^{2-}) is formed. Then, the dianion UA^{2-} will transfer an electron to the oxygen molecule (O_2) to activate the O_2. Starting from the activated O_2 (radical O_2^-), there are two possible pathways (Scheme 1), including the peroxide-

dependent Path A[11a,11e] and peroxide-independent Path B,[11b] for subsequent reactions steps. The second stage of the UA reaction in uricase is the hydration of dehydrourate, resulting in the product 5-hydroxyisourate. Furthermore, we should examine two possible pathways, including one leading to 5-HIU′[11g] and the other leading to 5-HIU which was confirmed in experiment[13–14] as the product of this stage.

Although there have been reports of pure quantum mechanical (QM) calculations[11a,11b,15] on the model reaction systems for studying the cofactor-free oxidase- and oxygenase-catalyzed reaction pathways, to our best of knowledge, no first-principles quantum mechanical/molecular mechanical (QM/MM) study on the detailed mechanism of the uricase-catalyzed oxidation of uric acid has been reported. Here we report the first QM/MM study on the detailed reaction pathways for uricase-catalyzed oxidation of UA, demonstrating novel mechanistic insights that could be valuable for understanding the general catalytic mechanisms of the cofactor-free oxidases- and oxygenases.[16] Specifically, first-principles QM/MM-free energy (QM/MM-FE) calculations were performed to uncover the detailed reaction pathways and the corresponding free energy profiles for uricase-catalyzed oxidation and hydration of UA. In these QM/MM-FE calculations, the QM/MM reaction-coordinate calculations were followed by free energy perturbation (FEP) calculations on the protein environment to account for the dynamic effects of the protein environment on the free energy barriers for the enzymatic reaction. Our QM/MM simulations were based on the pseudobond first-principles QM/MM approach,[17] which has been demonstrated to be a powerful tool in simulating a variety of enzymatic reactions,[18] and some theoretical predictions were subsequently confirmed by experimental studies.[18d,18e] The computational results clearly reveal the detailed reaction pathways and the corresponding free energy profiles for the uricase-catalyzed oxidation and hydration of UA. The rate-determining step is identified, and the roles of essential residues are discussed based on the QM/MM-optimized geometries for each catalytic reaction step.

Methods

Preparation of Initial Structures

In order to explore the reaction mechanism of uricase-catalyzed oxidation stage of UA, the initial enzyme-substrate ($ES1^t$) binding structure for uricase-8-HX complex was based on the neutron crystal structure of 8-HX binding with uricase (PDB entry as 4N9M with a resolution of 2.30 Å).[11g] We note that superscript “t” represents the triplet state, whereas superscript “s” represents the singlet. As indicated in literature, the uricase-catalyzed reaction involves the deprotonation of the substrate UA (*i.e.* 8-HX) and release of the H_2O_2 from the catalytic site. Notably, as shown in Scheme 2, the amine group on the Lys9 side chain of the uricase in the $ES1^t$ structure existed in a deprotonated state, as revealed in the neutron crystal structure of the uricase-8-HX complex. The atomic charges for 8-HX used in subsequent QM/MM calculations were the restrained electrostatic potential (RESP) charges. These RESP charges were determined by performing *ab initio* electrostatic potential calculations at the HF/6-31G* level using the Gaussian03 program,[19] followed by fitting with the standard RESP procedure implemented in the Antechamber module of the AMBER 11 program.[20] The ff03 force field[21] was used for uricase and the generalized Amber force

field (GAFF) for the substrate. Structurally, uricase is a homo-tetramer and contains four equal substrate-binding sites at the interface of each two neighboring subunits. As all the four binding sites are structurally similar, the initial structure of $ES1^t$ was constructed by retaining only two subunits of the tetramer, and the reaction-coordinate calculations were focused on one of the two binding sites. The system was neutralized by adding Na^+ ions as the counter ions and solvated in an orthorhombic box of TIP3P water molecules[22] with a minimum solute-wall distance of 10 Å. Once the whole system was set up, a series of energy minimizations and then a ~2 ns MD simulation was carried out by using the Sander module of Amber 11 program,[20] to make sure that there were no any significant changes in the structure after the MD simulation.

The last snapshot of the MD simulation was close to the average structure in the MD simulation and, thus, was used to prepare the initial structure of the first-principles QM/MM calculations. As we were only interested in the reaction center, the water molecules beyond 50 Å of the N^1 atom (Scheme 1) of the substrate were removed, leaving the QM/MM system for uricase-8-HX complex with 4,505 water molecules (23,013 atoms in total) for the oxidation reaction system neutralized with Na^+ counter ions. The QM/MM interface was treated by using a pseudobond approach.[17b,17d] Prior to the QM/MM geometry optimization, the initial reaction system was energy-minimized with the MM method by using the AMBER 11 program,[20] and a convergence criterion for energy gradient of 0.1 $kcal{\cdot}mol^{-1}{\cdot}Å^{-1}$ was achieved.

The binding structure for the hydration stage ($ES2^s$ and $ES2^{s'}$ in Scheme 3) of uricase-catalyzed reaction was prepared by taking advantage of the QM/MM-optimized structure of $INT3^s$ (Scheme 2) from the oxidation stage. The H_2O_2 in the structure of $INT3^s$ was replaced by a H_2O molecule, and the newly built binding structure was subject to the energy minimization and MD simulation in a similar way as that for the initial uricase-8-HX binding structure in the oxidation stage, and then was subject to the QM/MM geometry optimization.

Minimum-Energy Path of the Enzymatic Reaction

With a reaction-coordinate driving method and an iterative energy-minimization procedure,[18d] the enzyme reaction path was determined by the pseudobond QM/MM calculations at the B3LYP/6-31G*:AMBER level in which the QM calculations were performed at the B3LYP/6-31G* level of theory by using a modified version of Gaussian03 program,[19] and the MM calculations were performed by using a modified version of the AMBER8 program.[23] In addition, single-point energy calculations were carried out at the QM/MM(B3LYP/6-31+G*:AMBER) level on the QM/MM-optimized geometries. Throughout the QM/MM calculations, the boundary carbon atoms were treated with improved pseudobond parameters.[17b] No cutoff was used for non-bonded interactions in the QM/MM calculations. For the QM subsystem, the convergence criteria for geometry optimizations were the original Gaussian03 defaults, *i.e.* the maximum force of 0.53 $kcal{\cdot}mol^{-1}{\cdot}Å^{-1}$ (0.00045 au), the root-mean-squares (RMS) force of 0.35 $kcal{\cdot}mol^{-1}{\cdot}Å^{-1}$ (0.00030 au), the maximum displacement of 0.0018 au, and the RMS displacement of 0.0012 au. Normal mode analyses were performed to characterize the reactant,

intermediates, transition sates, and the final product. For the MM subsystem, the geometry optimization convergence criterion was achieved when the root-mean-squares deviation (RMSD) of energy gradient was ≤0.1 kcal·mol^{-1}·Å^{-1}. The atoms within 20 Å of N^1 atom of 8-HX (Scheme 1) were allowed to move freely while all of the other atoms outside this range were frozen during the QM/MM calculations.

Free Energy Perturbation

After the minimum-energy path was determined by the QM/MM calculations, the free energy changes associated with the QM-MM interactions were determined by using the free energy perturbation (FEP) method.[18b,18e] In the FEP calculations, sampling of the MM subsystem was carried out with the QM subsystem frozen at different states along the reaction path. The point charges on the frozen QM atoms used in the FEP calculations were those determined by fitting the electrostatic potential (ESP) in the QM part of the QM/MM single-point calculations. The total free energy difference between the transition state and the reactant was calculated with the same procedure used in our previous studies on other reaction systems.[18a,18f,18g,24] The FEP calculations enabled us to more reasonably determine relative free energy changes due to the QM-MM interactions. Technically, the final (relative) free energy determined by the QM/MM-FE calculations is the QM part of the QM/MM energy (excluding the Coulombic interaction energy between the point charges of the MM atoms and the ESP charges of the QM atoms) plus the relative free energy change determined by the FEP calculations. In the FEP calculations, the time step was 2 fs, and bond lengths involving hydrogen atoms were fixed. In sampling of the MM subsystem by MD simulations, the temperature was maintained at 298.15 K. Each FEP calculation consisted of 50 ps of equilibration and 300 ps of production sampling. Technically, the final relative free energy was taken as the average of the "forward" and "backward" perturbation results with the error bar being a half of the difference between the "forward" and "backward" perturbation results.

Most of the MD simulations and pseudobond QM/MM-FE calculations were performed on a supercomputer (*i.e.* the Dell X-series Cluster with 384 nodes or 4,768 processors) at the University of Kentucky Center for Computational Sciences. Some other modeling and computations were carried out on SGI workstations in our own laboratory.

Experimental methods

The experimental methods used in this study are similar to what we previously described.[25] Briefly, the pET28a vector was used for *Bacillus fastidiosus* uricase and its mutants including Asn271Leu or Gln299Ile mutation (generated by site-directed mutagenesis). The proteins were expressed in *Escherichia coli* BL21 (DE3), and cells collected for each protein (wild-type or mutant) were broken in a lysis buffer (20 mM Tris-HCl at pH 8.0) by sonication treatment (30% amplitude, 4-s treatment at 5-s intervals). The enzyme (wild-type or mutant) was purified by chromatography with DEAE-cellulose twice. The enzyme activity assays were performed by using the cell lysates first for the initial screening (in combination with an immunoturbidimetric assays that determines the enzyme concentration in the lysate), and then the purified enzyme for further verification. To measure the enzyme activity using a 96-well plate for each enzyme (wild-type or mutant), each well contained 20

μL diluted enzyme solution and 180 μL substrate (uric acid) solution. The absorbance at 293 nm was measured in 15.0 min at intervals of 1.0 min using a BioTek EON microplate reader. The absorbance data were used to estimate initial rate of the enzymatic reaction for a given substrate concentration, allowing to determine the maximal reaction rate (V_{max}) for each enzyme (wild-type or mutant).

Results and Discussion

The final RMSD of the reaction system compared to the original neutron crystal structure after the 2 ns of MD equilibration was 1.4 Å. Starting from the equilibrated system, further QM/MM reaction-coordinate calculations revealed the detailed reaction pathways. In general, the uricase-catalyzed reaction of UA consists of two stages, *i.e.* the oxidation stage starting from the bound 8-HX, and then the hydration stage. Various possible catalytic reaction pathways were explored by performing a series of QM/MM reaction-coordinate calculations as proposed in Schemes 2 and 3. Below we describe the structural details of the calculated reaction pathways and the obtained free energy profiles for both reaction stages.

Stage 1: Uricase-Catalyzed Oxidation of 8-HX

Fundamental Reaction Pathway—Starting from our QM/MM-optimized Michaelis-Menten complex of uricase-8-HX binding structure, we performed QM/MM reaction-coordinate calculations at the B3LYP/6-31G*:AMBER level. As shown in Figure 1A, atoms colored in blue were treated by QM method in the pseudobond first-principles QM/MM calculations. The QM region includes all atoms of substrate 8-HX and the triplet O_2 molecule, a water molecule, atoms from C^{ε} to the remaining part on the side chain of residue Lys9, atoms from C^{β} atom to all the remaining part on the side chain of residue Thr69, atoms from C^{β} atom to all the remaining part on the side chain of residue Asn271, and atoms from C^{γ} atom to all the remaining part on the side chain of residue Gln299. The boundary atoms colored red in Figure 1A were treated with improved pseudobond parameters.[17b] These boundary atoms were the C^{δ} atom on the side chain of residue Lys9, C^{α} atom of residue Thr69, C^{α} atom of residue Asn271, and the C^{β} atom of residue Gln299. All of the other atoms of uricase, the solvent water molecules, and the counter ions were treated as the MM subsystem.

The QM/MM reaction-coordinate calculation started from the enzyme-substrate (ES) complex structure with a triplet electronic state (denoted as $ES1^{t}$ in which superscript "t" will always represent a triplet electronic state throughout this report) for the QM region. The obtained results revealed that the uricase-catalyzed oxidation of 8-HX consists of four reaction steps. Figure 1B to F depict the QM/MM-optimized geometries of the reactant (Figure 1B), intermediates, transition states of the first and second steps of the oxidation stage of uricase-catalyzed reaction for 8-HX. The first step is the proton transfer from substrate 8-HX to N^{z} atom of residue Lys9 assisted by residue Thr69, along with an electron transfer from the substrate to the oxygen molecule to activate the oxygen molecule. The second reaction step is the proton transfer from the protonated amino group of residue Lys9 to the O^{2} atom of the activated oxygen molecule, which results in the diradical

recombination between the C^5 atom of substrate and O^1 atom of the oxygen molecule to form the C^5-O^1 bond. The next reaction step is the dissociation of H_2O_2 molecule.

Step 1. Proton H^{14} Transfer from O^{10} Atom of 8-HX to N^z Atom of Lys9 Mediated by Hydroxyl Group of Thr69: Figure 1B depicts the QM/MM-optimized uricase–8-HX binding structure. The distance from the center of the six-membered ring of 8-HX to the aromatic side chain of residue Phe179 of uricase is 3.351 Å, indicating strong π-π stacking interactions. The distances for hydrogen-bonding interactions between the six-membered ring of substrate 8-HX and residues Arg196 and Gln245 of uricase are all shorter than 1.900 Å, suggesting that 8-HX is well anchored in the binding site of uricase. The hydroxyl group on the side chain of residue Thr69 acts as a hydrogen-bonding bridge between the O^{10} atom (Figure 1B) of 8-HX and the -NH_2 group on the side chain of residue Lys9. A water molecule (W1) nearby Asn271 side chain is hydrogen-bonded with the -N^9-H^{16} group of 8-HX with an O···H distance of 2.124 Å. The O_2 molecule is held tightly by residues Asn271 and Gln299 through strong hydrogen-bonding interactions.

As shown in Scheme 2, the nature of chemical reaction step 1 can be represented by the changes of four internuclear distances (*i.e.* $R_{H14\text{-}O10}$, $R_{H\gamma\text{-}O\gamma}$, $R_{H\gamma\text{-}Nz}$, and $R_{O\gamma\text{-}H14}$). Therefore, $R_{H14\text{-}O10} + R_{H\gamma\text{-}O\gamma} - R_{H\gamma\text{-}Nz} - R_{O\gamma\text{-}H14}$ was set as the reaction coordinate for this first reaction step. As shown in the QM/MM-optimized geometries (Figure 1B to D), a proton gradually transfers from 8-HX to Thr69 and then to Lys9 during the reaction. Meanwhile, an electron transfers from 8-HX to the triplet oxygen molecule, with the transferred electron occupying an anti-π (π*) orbital of the oxygen molecule. As a result of the electron transfer (Figure 2), the spin density (SD) of the oxygen molecule changes from 1.83 in $ES1^t$ to 1.61 in $TS1^t$ and to 1.01 in $INT1^t$, while the SD value of 8-HX changes from 0.16 in $ES1^t$ to 0.39 in $TS1^t$ and to 0.99 in $INT1^t$. So, both the substrate and O_2 become radicals after the first step of the reaction, which is consistent with the experimental findings[11c,26] that the electron spin resonance spectroscopy (ESR) studies were able to trap substrate radical.

Our computational results indicate that the first reaction step actually produces $INT1^t$ (which a radical substrate UA^- and a radical O_2^- in the active site) rather than $INT1^{t\prime}$ (UA^{2-} dianion and triplet O_2 in the active site) depicted in Scheme 2. We should note that the electronic structure state of the reaction system was determined automatically during the QM part of the QM/MM calculations. There was no restriction concerning whether this reaction step should produce $UA^- + O_2^-$ or $UA^{2-} + O_2$ in our QM/MM calculations. In other words, the existence of $UA^- + O_2^-$ in the active site is the outcome of the QM/MM calculations, rather than the assumption. So, the enzyme active site favors $UA^- + O_2^-$ as compared to $UA^{2-} + O_2$. Based on the negative ionization potentials of urate dianions calculated by Altarsha *et al.*,[27] UA^{2-} can easily transfer one electron to O_2; however, the electron transfer is independent of the proton transfer, which is not the case for urate monoanion like the reactant here. Our computational finding is different from the popularly recognized mechanism[11f] that the substrate (UA) will first become a dianion (UA^{2-}) and then transfer an electron to O_2. According to our computational results, the UA^{2-} dianion will not exist at all in the active site under aerobic condition, because it can automatically transfer an electron to the nearby O_2 molecule and activate the O_2 molecule. As a result of

the O_2 activation, the O–O distance ($R_{O1\text{-}O2}$) in the oxygen molecule changes from 1.230 Å in $ES1^t$ to 1.258 Å in $TS1^t$ and to 1.337 Å in $INT1^t$. Correspondingly, as shown in Figure 1B to D, $R_{H14\text{-}O10}$ elongates from 1.013 Å in $ES1^t$ to 1.515 Å in $TS1^t$ and to 3.254 Å in $INT1^t$, $R_{O\gamma\text{-}H\gamma}$ elongates from 1.005 Å in $ES1^t$ to 1.283 Å in $TS1^t$ and then to 1.484 Å in $INT1^t$, $R_{H14\text{-}O\gamma}$ shortens from 1.629 Å in $ES1^t$ to 1.051 Å in $TS1^t$ and then to 1.046 Å in $INT1^t$, and $R_{Nz\text{-}H\gamma}$ shortens from 1.726 Å in $ES1^t$ to 1.233 Å in $TS1^t$ and then to 1.113 Å in $INT1^t$.

As noted above, the first reaction step produces $UA^- + O_2^-$, rather than $UA^{2-} + O_2$, due to the automatic electron transfer from UA^{2-} to O_2 coupled with the O_2 activation. The O_2 activation is associated with the increase in the O–O bond length ($R_{O1\text{-}O2}$). To further test this point, we also re-carried out the aforementioned QM/MM reaction-coordinate calculations, but with the O–O bond length ($R_{O1\text{-}O2}$) frozen at that (~1.230 Å) in the optimized $ES1^t$ structure. We expected that O_2 would not accept an electron from UA^{2-} when the O–O bond length was frozen. Not surprisingly, the QM/MM reaction-coordinate calculations with $R_{O1\text{-}O2}$ frozen indeed led to $UA^{2-} + O_2$ in the active site, but with a significantly higher energy barrier (see Supporting Information for the detailed results), which further supports the conclusion that the reaction pathway *via* $UA^- + O_2^-$, rather than $UA^{2-} + O_2$, is the more favorable pathway.

It should be pointed out that the above conclusion concerning the electronic structure states $UA^- + O_2^-$ and $UA^{2-} + O_2$ should be limited to that in the active site of uricase during the uricase-catalyzed oxidation of uric acid. The non-enzymatic reaction of uric acid could be completely different. In fact, the urate dianion (UA^{2-}) was detected in multiple experimental observations for the non-enzymatic reaction of uric acid.[11b,28]

Further, we should also note that the aforementioned strong π-π stacking interaction between the six-membered ring of 8-HX and the aromatic side chain of residue Phe179 of uricase was based on the QM/MM reaction-coordinate calculations in which Phe179 was included on the MM region. In order to confirm this important π-π stacking interaction, we also repeated the QM/MM reaction-coordinate calculations for this reaction step by moving Phe179 from the MM region to the QM region. The new QM/MM calculations with Phe179 included in the QM region led to very similar detailed geometric and energetic results (that also revealed the strong π-π stacking interaction); see Supporting Information for the detailed data (Figures S5 and S6).

Step 2. Proton Transfer from the Positively Charged -NH_3^+ Group of Lys9 to O^2 Atom of Oxygen Molecule Mediated by Hydroxyl Group of Thr69: In this step, the proton (H^{14}) gradually transfers from the O^γ atom of Thr69 side chain to the O^2 atom of the oxygen molecule, while another proton (H^γ) gradually transfers from the N^z atom on the positively charged -NH_3^+ group of Lys9 to the O^γ atom of Thr69 side chain. So, $R_{H14\text{-}O\gamma} + R_{Nz\text{-}H\gamma} - R_{H14\text{-}O2} - R_{O\gamma\text{-}H\gamma}$ was set as the reaction coordinate for this reaction step. As shown in Figure 1D to F, $R_{H14\text{-}O\gamma}$ changes from 1.046 Å in $INT1^t$ to 1.077 Å in $TS2^t$ and to 1.569 Å in $INT2^t$, $R_{Nz\text{-}H\gamma}$ changes from 1.113 Å in $INT1^t$ to 1.162 Å in $TS2^t$ and then to 1.777 Å in $INT2^t$, $R_{H14\text{-}O2}$ shortens from 1.551 Å in $INT1^t$ to 1.456 Å in $TS2^t$ and to 1.030 Å in $INT2^t$, and $R_{O\gamma\text{-}H\gamma}$ shortens from 1.484 Å in $INT1^t$ to 1.383 Å in $TS2^t$ and then to 1.003 Å in $INT2^t$.

Step 3. Diradical Recombination to Form the C5–O1 Bond: As proposed in Scheme 2 (Path A), the OOH radical and the substrate radical in intermediate $INT2^t$ are recombined to form the singlet intermediate $INT2^s$ (Figure 3). During this recombination process, a single bond (C^5–O^1) is formed and the planar structure around the C^5 atom of the substrate gradually changes into a tetrahedral structure. Thus, C^5 atom changes from sp^2-hybridization to sp^3-hybridization in the peroxo intermediate $INT2^s$ (Figure 3B). Meanwhile, the C^5=C^4 double bond changes gradually to a single bond. This change is compensated by the formation of C^4=N^3 double bond. The hydrogen bonding interaction between the O^1 atom of O_2 molecule and the H^δ atom on the amide group of Gln299 side chain is replaced by a new hydrogen bond between the O^2 atom of O_2 molecule and the H^δ atom at Gln299 side chain.

In fact, starting from the QM/MM-optimized $INT2^t$ geometry, further QM/MM geometry optimization after changing the triplet state to the singlet state automatically went to the $INT2^s$ geometry without an energy barrier, suggesting that the transition from the $INT2^t$ state to the $INT2^s$ state is likely a spontaneous process. We also tried to explore alternative reaction pathways without changing the triplet state to the singlet state, and found that the C^5–O^1 bond can never form when the reaction system was kept at the triplet state; there was no transition state associated with the C^5–O^1 bond formation in the triplet state. In addition, we also tried to locate another hypothetical transition state $TS3^t$ (Path B) depicted in Scheme 2 and concluded that this pathway is unlikely because the energy always became higher and higher without a saddle point on the potential energy surface along the hypothetical reaction path. It should be noted that, in principle, inability to locate a saddle point in a computational study is no proof of its nonexistence. On the other hand, in this particular case, a reasonable alternative pathway (Path A) has been identified and it is not the rate-determining step in the overall reaction. Path B is probably a high-energy one, even if it does exist, and thus there is no point investigating this further. Noteworthy, we also calculated the Raman spectrum of QM/MM-optimized $INT2^s$, and found a ~602 cm^{-1} band; the calculated band of ~602 cm^{-1} is very close to the experimentally observed band of 605 cm^{-1} in the peroxo intermediate.[11f]

The C^5–O^1 distance (3.673 Å) in the triplet intermediate $INT2^t$ shortens to 1.537 Å in the singlet intermediate $INT2^s$, while the O^1–O^2 distance elongates from 1.330 Å in the triplet intermediate $INT2^t$ to 1.440 Å in $INT2^s$. We calculated the energy profiles associated with both the triplet and singlet states, showing the crossing point when the distance $R_{C5–O1}$ = ~3.280 Å (see below for the energy profiles). At the end of this reaction step, the substrate bears −1e charge, and a hydrogen-bonding network is formed between the O^1 atom, the water molecule (W1), and the amide group on Asn271 side chain.

Step 4. Dissociation of H_2O_2: Starting from the structure of the singlet intermediate $INT2^s$ (Figure 3B), the C^5–O^1 bond breaking is coupled with the proton (H^{16}) transfer from N^9 to O^1, assisted by a water molecule (W1), leading to the dissociation of H_2O_2 from the catalytic site. $R_{C5\text{-}O1} + R_{Hw\text{-}Ow} + R_{N9\text{-}H16} - R_{Hw\text{-}O1} - R_{H16\text{-}Ow}$ was set as the reaction coordinate. As shown in Figure 3, $R_{C5\text{-}O1}$ changes from 1.537 Å in $INT2^s$ to 2.657 Å in $TS3^s$ and to 2.951 Å in $INT3^s$, $R_{Hw\text{-}Ow}$ changes from 0.979 Å in $INT2^s$ to 1.292 Å in $TS3^s$ to 1.862 Å in $INT3^s$, $R_{N9\text{-}H16}$ changes from 1.012 Å in $INT2^s$ to 1.068 Å in $TS3^s$ and then to

1.782 Å in $INT3^s$, R_{Hw-O1} shortens from 1.914 Å in $INT2^s$ to 1.158 Å in $TS3^s$ and to 0.986 Å in $INT3^s$, and R_{H16-Ow} shortens from 3.784 Å in $INT2^s$ to 1.662 Å in $TS3^s$ and then to 1.001 Å in $INT3^s$. As the H^w atom from the water molecule gradually approaches the O^1 atom of the OOH group in the catalytic site, the C^5-O^1 bond in the substrate is gradually weakened. The C^5–O^1 bond breaks down when the H^w–O^1 bond is formed. Corresponding to this proton transfer, the sp^3-hybridized C^5 ($INT3^s$) changes back to sp^2-hybridization. After the C^5=N^7 double bond is formed in $INT3^s$ (as proposed in Scheme 2), all the atoms of the substrate become co-planar. Consequently, the product dehydrourate is generated, and the H_2O_2 molecule is released from the reaction center.

Stage 2: Uricase-Catalyzed Hydration of the Intermediate Dehydrourate

So far, the uricase-catalyzed oxidation stage of 8-HX produced the intermediate dehydrourate. After the release of H_2O_2 molecule from the reaction center, the catalytic reaction entered the second stage for the hydration of dehyrourate. In the QM/MM-optimized uricase-dehydrourate binding structure ($ES2^s$ or $ES2^{s'}$), there are two possible pathways to form the different products as proposed in Scheme 3.

As shown in Figure 4 for the results from our QM/MM calculations, a water molecule was identified as a nucleophile to attack C^5 atom of dehydrourate. In addition, a strong hydrogen-bonding network was formed among the $–NH_3^+$ group on Lys9 side chain, hydroxyl group on Thr69 side chain, a water molecule, and the N^7 atom of dehydrourate (Figure 4B). The distance between the oxygen atom (O^w) of a water molecule and C^5 atom of dehydrourate is 2.797 Å in the $ES2^s$ binding structure, which is ideal for the potential nucleophilic attack. As O^w atom of water gradually approaches C^5 atom of dehydrourate during the nucleophilic attack, H^w atom of water comes close to the hydroxyl oxygen (O^γ atom) on Thr69 side chain. Meanwhile, the H^γ atom of the hydroxyl group on Thr69 side chain gradually forms a bond with the N^7 atom of dehydrourate, changing the C^5=N^7 double bond to a single bond (as proposed in Scheme 3). The chemical nature of this reaction stage can be represented by the changes of the distances R_{C5-Ow}, R_{Ow-Hw}, $R_{O\gamma-Hw}$, $R_{O\gamma-H\gamma}$, and $R_{N7-H\gamma}$. Thus, the reaction coordinate was set as $R_{Ow-Hw} - R_{C5-Ow} + R_{O\gamma-H\gamma} - R_{O\gamma-Hw} - R_{N7-H\gamma}$ for this hydration stage. In changing from $ES2^s$ to EP^s through the transition state $TS4^s$ (Figure 4C), the coplanar geometry around C^5 atom changes to a tetrahedral geometry, and the C^5 atom itself changes from sp^2-hybridization to sp^3-hybridization. The QM/MM-optimized geometry of EP^s (Figure 4D) shows that the nucleophilic attack process is completed after the –OH group of water is bonded with C^5 atom and the concerted proton transfer is completed. Once the product 5-hydroxyisourate is released from the active site, the whole reaction of uricase-catalyzed oxidation and hydration of UA is completed. Furthermore, we placed the water molecule in the proper position for nucleophilic attack on C^4 atom of substrate (*i.e.* the distance of C^4-O^w was ~2.1 Å, which is similar to that in $TS4^s$), and found that the distance between O^w atom of water and O^g atom of T69 residue became much longer (>4.0 Å), suggesting that the proton transfer between water and substrate *via* T69 residue would be very difficult to occur. So we may reasonably conclude that the attack on C5 atom rather than C4 atom by water should be more favorable in the hydration stage.

In addition, another possible hydration pathway of dehydrourate leading to product $EP^{s\prime}$ was explored, and the corresponding structures of stationary points are depicted in Figure 5. In this pathway, $R_{Ow1\text{-}Hw1} + R_{Ow2\text{-}Hw2} - R_{C5\text{-}Ow1} - R_{Ow2\text{-}Hw1} - R_{N9\text{-}Hw2}$ was set as the reaction coordinate for this reaction stage. As shown in Figure 5, $R_{Ow1\text{-}Hw1}$ changes from 0.981 Å in $ES2^{s\prime}$ to 1.177 Å in $TS4^{s\prime}$ and to 1.881 Å in $EP^{s\prime}$, $R_{Ow2\text{-}Hw2}$ changes from 0.988 Å in $ES2^{s\prime}$ to 1.672 Å in $TS4^{s\prime}$ and to 3.819 Å in $EP^{s\prime}$, $R_{C5\text{-}Ow1}$ shortens from 2.653 Å in $ES2^{s\prime}$ to 2.309 Å in $TS4^{s\prime}$ and to 1.470 Å in $EP^{s\prime}$, $R_{Ow2\text{-}Hw1}$ shortens from 1.881 Å in $ES2^{s\prime}$ to 1.274 Å in $TS4^{s\prime}$ and to 0.980 Å in $EP^{s\prime}$, and $R_{N9\text{-}Hw2}$ shortens from 1.877 Å in $ES2^{s\prime}$ to 1.071 Å in $TS4^{s\prime}$ and then to 1.012 Å in $EP^{s\prime}$.

Alternative Reaction Pathway without Participation of Residues Lys9 and Thr69 in the chemical reaction process

In addition to the main reaction pathways (Schemes 2 and 3) with participation of Lys9 and Thr69 in the chemical reaction process, we also tried to explore possible alternative reaction pathways without participation of Lys9 and Thr69 in the chemical reaction process. Scheme 4 shows a possible alternative pathway identified for the oxidation and hydration processes (see Supporting Information for the geometric data obtained from the QM/MM calculations).

Free Energy Profiles

For all of explored possible pathways of the uricase-catalyzed oxidation and hydration of UA, we wanted to determine the free energy profiles for all of these uricase-catalyzed reaction pathways and know the rate-determining step. For this purpose, we performed QM/MM single-point energy calculations at the B3LYP/6-31+G*:AMBER level for each QM/MM-optimized geometry along the minimum-energy path for both oxidation and hydration stages. For all atoms of each optimized geometry along the reaction path, the ESP charges determined in the QM part of the QM/MM single-point energy calculation were used in the subsequent FEP simulations to estimate the free energy changes. Depicted in Figures 6 and 7 are the free energy profiles for uricase-catalyzed oxidation and hydration of UA, which were determined by the QM/MM-FE calculations with the zero-point and thermal corrections for the QM subsystem. As seen in the figure, the error bars reflecting the differences between the “forward” and the “backward” perturbations were all reasonably small, suggesting that the FEP calculations converged well in terms of the numeric computations within the FEP windows used.

As shown in Figure 6, the free energy barriers calculated for the reaction steps 1, 2, and 4 of the uricase-catalyzed oxidation of 8-HX are 10.0, 0.8, and 13.3 kcal/mol, respectively. Based on these free energy barriers, reaction step 4 has the highest free energy barrier in the oxidation stage of the catalytic reaction. It should be noted that the step 3 (radical recombination) is actually a barrierless process, and there is a crossing point between the energy surface of the triplet state and that of the singlet state. As shown in Figure 7, the free energy barrier for uricase-catalyzed hydration pathway leading to product EP^{s} (16.2 kcal/mol) or $EP^{s\prime}$ (22.1 kcal/mol) is even higher than all of the free energy barriers in the oxidation stage, indicating that the hydration stage of 8-HX is rate-determining. Based on the calculated free energy profiles (Figure 7) for the hydration stage of the uricase-catalyzed

reaction of 8-HX, the dominant product should be the 5-HIU in EP^{s}, rather than the 5-HIU′ in $EP^{s'}$, as the difference between these two free energy barriers is as high as 5.9 kcal/mol. Our computational data are consistent with the experimental observation of the product.[13–14]

As shown in Figure 8, the free energy barriers for the alternative pathway (without participation of Lys9 and Thr69 in the chemical reaction process) depicted in Scheme 4 are 11.5 kcal/mol (for the reaction step associated with transition state $TS1^{t''}$) and 19.2 kcal/mol (for the reaction step associated with transition state $TS4^{s''}$). The data suggest that, for the alternative reaction pathway, the hydration stage is still the rate-determining step with an energy barrier which is 3.0 kcal/mol higher than that (16.2 kcal/mol) *via* $TS4^{s}$.

The mechanistic insights into the catalytic reaction pathways and the calculated free energy profiles for the entire uricase-catalyzed oxidation and hydration of UA can be used to better understand previous experimental observations.[11d,11e,11h–11j,29] For example, as observed from site-directed mutagenesis studies on *Bacillus subtilis* uricase,[11d,29] the Lys9Met, Thr69Ala, Thr69Val, or Lys9Met/Thr69Ala mutation(s) resulted in a dramatic decrease of the maximum rate of the catalytic reaction (V_{max}) from 3.26 s^{-1} for the wild-type enzyme to nearly zero for each of these mutants. As discussed above, residues Lys9 and Thr69 of uricase play a critical role in the proton transfers during the oxidation and hydration stages of the catalytic reaction process for the most favorable reaction pathway. Mutations on these two residues will disrupt the concerted proton transfer process and, thus, considerably slow down the catalytic reaction process. On the other hand, mutations of Lys9 and/or Thr69 may not completely inactivate the enzyme, due to the existence of the alternative pathway without participation of Lys9 and Thr69 residues in the chemical reaction process. The computational insights are qualitatively consistent with the experimental observations[11d] demonstrating that the Thr69Ala mutant has a V_{max} that is 3% of the wild type, and the Lys9Met mutant has a V_{max} that is 0.4% of the wild type.

Further, as reported,[11e] the experimentally measured rate constant (k_{cat}) for uricase-catalyzed oxidation of UA ranges from 6.0 s^{-1} to 70 s^{-1} at T = 298.15 K for uricase. The k_{cat} value can be used to estimate the free energy barrier ($\Delta G^{\neq}$) for uricase-catalyzed oxidation and hydration of UA. According to classic transition state theory, [30] we have

$$k_{\mathrm{cat}}=k_b T/h\exp(-\Delta G^{\neq}/RT) \quad (1)$$

where k_b is the Boltzmann's constant, h is the Planck constant, and T is the temperature. In Eq. (1), $\Delta G^{\neq}$ is the overall free energy barrier for the enzymatic reaction. According to Eq. (1), $\Delta G^{\neq}$ can be calculated as

$$\Delta G^{\neq}=-RT\ln(\frac{k_{cat}h}{k_b T}). \quad (2)$$

Using the experimentally measured k_{cat} values of 6.0 ~ 70 s^{-1} for uricase-catalyzed oxidation and hydration of UA, we obtained $\Delta G^{\neq}$= 16.4 ~ 14.9 kcal/mol. This value of free energy barrier derived from experimental measurements is close to our free energy barrier (16.2 kcal/mol) calculated for the rate-determining step of the uricase-catalyzed reaction. The consistency between the calculated free energy barrier for uricase-catalyzed oxidation of UA and available experimental kinetic data suggests that our computationally revealed fundamental reaction pathways and the free energy profiles are reasonable and reliable.

Implication for Rational Design of Uricase Mutants with Improved Catalytic Activity

In order to design novel mutants of uricase with improved catalytic activity for UA, one needs to find amino-acid mutation(s) that can accelerate the rate-determining step of the entire catalytic reaction while all the other steps are not significantly affected by the designed mutation(s). Based on the above-discussed catalytic reaction pathway and the related free energy profile, the rate-determining step is the hydration of dehydrourate. Therefore, computational design of the desirable mutants of uricase should be focused on this rate-determining step. According to the QM/MM-calculated favorable reaction pathway, the nucleophilic attack of a water molecule on C^5 atom of dehydrourate is coupled by proton transfer among the attacking water molecule, the hydroxyl group on Thr69 side chain, and the N^7 atom of dehydrourate. Theoretically, any mutations that can help to stabilize $TS4^s$ structure (Figure 4C) will likely decrease the free energy barrier for the transformation of dehydrourate to 5-hydroxyisourate. A detailed analysis of QM/MM-optimized geometries suggests that the high free energy barrier for the hydration reaction stage may be attributed to the weak binding of water molecule in the catalytic site.

As visually inspected on the $ES2^s$ complex, the bound water molecule is not strongly hydrogen-bonded with its possible partners Thr69, Asn271, and Gln299. The hydrogen atom of the water molecule is 2.214 Å from the hydroxyl oxygen atom at Thr69 side chain (Figure 4B), suggesting that this hydrogen-bonding interaction is weak. The oxygen atom of the water molecule is 2.435 Å from the H^{δ} atom at Asn271 side chain, and 3.416 Å away from the H^{e} atom at Gln299 side chain. In addition, the distance between the oxygen atom of water and the C^5 atom of dehydrourate in $ES2^s$ complex is also rather long (2.797 Å), making it harder to allow the nucleophilic attack by the water oxygen atom in this reaction stage. One possible way to shorten the distance for the nucleophilic attack is to improve the hydrogen-bonding interactions between the bound water molecule and its surrounding partners. Thus, certain mutations on residues Thr69, Asn271, and Gln299 that could enhance hydrogen-bonding interactions with the water molecule would worth a try for the purpose to lower the free energy barrier of the hydration reaction stage for uricase-catalyzed oxidation of UA.

On the other hand, as well known, computational design and discovery of a high-activity mutant of an enzyme are extremely challenging and labor-intensive, because a truly reliable mutant design must be based on more extensive QM/MM calculations on the free energy profiles of a variety of possible hypothetical mutants. So, before carrying out extensive computational design and experiments for the uricase redesign, we would like to make sure that Thr69, Asn271, and Gln299 are indeed key residues affecting the catalytic activity of

the enzyme. As discussed above, the importance of Thr69 has already been tested experimentally, but Asn271 and Gln299 are the newly identified key residues in this computational study. In order to verify the importance of Asn271 and Gln299, we examined the effects of Asn271Leu and Gln299Ile mutations on the catalytic activity (V_{max}) of *Bacillus fastidiosus* uricase by carrying out experimental studies including site-directed mutagenesis, protein expression, and the *in vitro* enzyme activity assays. The mutant and wild-type uricase enzymes were expressed and assayed at the same time under the same experimental conditions, in order to reasonably compare their activity (V_{max}). Based on the interaction model discussed above, the Gln299Ile and Asn271Leu mutations may potentially disrupt their hydrogen-bonding interactions with the O_2 and water molecule and, thus, decrease the catalytic activity of the enzyme. According to the *in vitro* experimental data, with the Asn271Leu mutation, the uricase activity was too low to be detected (or with V_{max} < 1% of the V_{max} for the wild-type enzyme) within the detection limit of our activity assay. The Gln299Ile mutation also significantly decreased the V_{max} of the enzyme by ~13 fold; the Gln299Ile mutant had ~8% activity compared to the wild-type uricase. Our new experimental data are consistent with the computationally revealed roles of Asn271 and Gln299 in the enzymatic reaction process.

In addition, we also prepared and tested the Lys9His, Lys9Arg, and Lys9Glu mutants, and found that none of these mutants was active within the detection limit. These results further support the crucial role of Lys9 in the catalysis, as revealed by our computational study.

Conclusion

Pseudobond first-principles QM/MM-FE calculations carried out in this study have demonstrated the detailed reaction pathways for uricase-catalyzed reaction of UA. Based on the results obtained from the QM/MM-FE calculations, the uricase-catalyzed reaction consists of two distinct stages, *i.e.* the oxidation and hydration. In the oxidation stage, substrate 8-HX was transformed to the intermediate dehydrourate. The oxidation of 8-HX was initiated by proton transfer from 8-HX to the side chain of Lys9, which was assisted by hydroxyl group of Thr69, along with an electron transfer from the substrate to the oxygen molecule so as to activate the oxygen molecule. Hence, the initial reaction step produces a radical substrate UA^- and a radical O_2^- in the active site. The initial reaction step is followed by another proton transfer from the protonated -NH_3^+ group on Lys9 side chain to the O_2^- radical. Then, it is a diradical recombination process. The oxidation of 8-HX is finished by the fourth step as the dissociation of H_2O_2 molecule. The free energy barrier for the fourth reaction step (dissociation of H_2O_2) in the oxidation stage is 13.3 kcal/mol. There are two main reaction pathways in hydration stage of the catalytic reaction, and the most favorable one is initiated by the nucleophilic attack on the dehydrourate by a water molecule in the catalytic site, and coupled by a concerted proton transfer among the substrate, a bound water molecule, and the hydroxyl group on Thr69 side chain. The free energy barrier for the hydration stage of the catalytic reaction is 16.2 kcal/mol, making this stage as the rate-determining step for the entire catalytic reaction. The calculated overall free energy barrier of 16.2 kcal/mol is close to that (16.4 to 14.9 kcal/mol) derived from available experimental kinetic data, suggesting that the computationally determined catalytic reaction mechanism is reasonable. The novel mechanistic insights provide a mechanistic base for future rational

design of uricase mutants with improved catalytic activity against uric acid as an improved enzyme therapy.

Notably, our computational finding is different from the popularly recognized mechanism that the substrate (UA) will first become a dianion (UA^{2-}) and then transfer an electron to O_2. According to our computational results, the UA^{2-} dianion will not exist at all in the active site under aerobic condition. Further, the novel mechanistic insights into the catalytic mechanism of uricase should be invaluable in understanding catalytic mechanisms for numerous other cofactor-free oxidase-catalyzed reactions involving an oxygen molecule.

Supplementary Material

Refer to Web version on PubMed Central for supplementary material.

Acknowledgments

This work was supported in part by the National Science Foundation (NSF grant CHE-1111761), National Institutes of Health (NIH grant UL1 TR000117: University of Kentucky Center for Clinical and Translational Science), National Natural Science Foundation of China (Nos. 21303167 and 21403199), and China Postdoctoral Science Foundation (Nos. 2013M530340 and 2015T80776). The authors also acknowledge the Center for Computational Sciences (CCS) at the University of Kentucky for supercomputing time on a Dell X-series Cluster with 384 nodes or 4,768 processors.

References

1. Kennedy LD, Ajiboye VO. J Oncol Pharm Pract. 2010; 16:205–213. [PubMed: 19923162]
2. (a) Sevanian A, Davies KJ, Hochstein P. Am J Clin Nutr. 1991; 54:1129S–1134S. [PubMed: 1962559] (b) Kaltwasser H. J Bacteriol. 1971; 107:780–786. [PubMed: 5095289]
3. Wu XW, Muzny DM, Lee CC, Caskey CT. J Mol Evol. 1992; 34:78–84. [PubMed: 1556746]
4. (a) Zhao Y, Zhao L, Yang G, Tao J, Bu Y, Liao F. Biotechnol Appl Biochem. 2006; 45:75–80. [PubMed: 16689679] (b) Zhao Y, Yang X, Li X, Bu Y, Deng P, Zhang C, Feng J, Xie Y, Zhu S, Yuan H, Yu M, Liao F. Biosci Biotechnol Biochem. 2009; 73:2141–2144. [PubMed: 19734651] (c) Zhang C, Yang X, Feng J, Yuan Y, Li X, Bu Y, Xie Y, Yuan H, Liao F. Biosci Biotechnol Biochem. 2010; 74:1298–1301. [PubMed: 20530883] (d) Feng J, Li X, Yang X, Zhang C, Yuan Y, Pu J, Zhao Y, Xie Y, Yuan H, Bu Y, Liao F. Arch Pharm Res. 2010; 33:1761–1769. [PubMed: 21116779]
5. (a) Pui CH. Expert Opin Pharmacother. 2002; 3:433–442. [PubMed: 11934348] (b) Richette P, Briere C, Hoenen-Clavert V, Loeuille D, Bardin T. J Rheumatol. 2007; 34:2093–2098. [PubMed: 17896799] (c) Bose P, Qubaiah O. J Clin Pharm Ther. 2011; 36:299–326. [PubMed: 21501203]
6. (a) Darmon M, Guichard I, Vincent F. J Clin Oncol. 2011; 29:e67–e68. [PubMed: 21149649] (b) Hussar DA, Pasco L. J Am Pharm Assoc. 2011; 51:316–319.
7. Yang X, Yuan Y, Zhan CG, Liao F. Drug Dev Res. 2012; 73:66–72. [PubMed: 22665944]
8. (a) Sherman MR, Saifer MG, Perez-Ruiz F. Adv Drug Deliv Rev. 2008; 60:59–68. [PubMed: 17826865] (b) Hershfield MS, Roberts LJ 2nd, Ganson NJ, Kelly SJ, Santisteban I, Scarlett E, Jaggers D, Sundy JS. Proc Natl Acad Sci USA. 2010; 107:14351–14356. [PubMed: 20660758]
9. (a) Zheng F, Xue L, Hou S, Liu J, Zhan M, Yang W, Zhan CG. Nat Commun. 2014; 5:3457. [PubMed: 24643289] (b) Xue L, Ko MC, Tong M, Yang W, Hou S, Fang L, Liu J, Zheng F, Woods JH, Tai HH, Zhan CG. Mol Pharmacol. 2011; 79:290–297. [PubMed: 20971807] (c) Pan Y, Gao D, Yang W, Cho H, Yang G, Tai HH, Zhan CG. Proc Natl Acad Sci USA. 2005; 102:16656–16661. [PubMed: 16275916] (d) Zheng F, Yang W, Xue L, Hou S, Liu J, Zhan CG. Biochemistry. 2010; 49:9113–9119. [PubMed: 20886866] (e) Liu JJ, Zhan CG. J Chem Theory Comput. 2012; 8:1426–1435. [PubMed: 23066354]
10. (a) Pitts OM, Priest DG. Biochemistry. 1973; 12:1358–1363. [PubMed: 4696756] (b) Sarma AD, Tipton PA. J Am Chem Soc. 2000; 122:11252–11253.(c) Tipton PA. Methods Enzymol. 2002;

354:310–319. [PubMed: 12418236] (d) Kahn K, Tipton PA. Biochemistry. 1997; 36:4731–4738. [PubMed: 9125493]

11. (a) Kahn K. Bioorg Chem. 1999; 27:351–362.(b) Altarsha M, Castro B, Monard G. Bioorg Chem. 2009; 37:111–125. [PubMed: 19539344] (c) Gabison L, Chopard C, Colloc'h N, Peyrot F, Castro B, El Hajji M, Altarsha M, Monard G, Chiadmi M, Prange T. Proteins. 2011; 79:1964–1976. [PubMed: 21491497] (d) Imhoff RD, Power NP, Borrok MJ, Tipton PA. Biochemistry. 2003; 42:4094–4100. [PubMed: 12680763] (e) Kahn K, Tipton PA. Biochemistry. 1998; 37:11651–11659. [PubMed: 9709003] (f) Bui S, von Stetten D, Jambrina PG, Prange T, Colloc'h N, de Sanctis D, Royant A, Rosta E, Steiner RA. Angew Chem, Int Ed. 2014; 53:13710–13714.(g) Oksanen E, Blakeley MP, El-Hajji M, Ryde U, Budayova-Spano M. PLoS One. 2014; 9:e86651. [PubMed: 24466188] (h) Gabison L, Chiadmi M, El Hajji M, Castro B, Colloc'h N, Prange T. Acta Crystallogr D Biol Crystallogr. 2010; 66:714–724. [PubMed: 20516624] (i) Colloc'h N, Gabison L, Monard G, Altarsha M, Chiadmi M, Marassio G, Sopkova-de Oliveira Santos J, El Hajji M, Castro B, Abraini JH, Prange T. Biophys J. 2008; 95:2415–2422. [PubMed: 18375516] (j) Gabison L, Prange T, Colloc'h N, El Hajji M, Castro B, Chiadmi M. BMC Struct Biol. 2008; 8:32. [PubMed: 18638417] (k) Colloc'h N, Girard E, Dhaussy AC, Kahn R, Ascone I, Mezouar M, Fourme R. Biochim Biophys Acta. 2006; 1764:391–397. [PubMed: 16478683]
12. Yamamoto K, Kojima Y, Kikuchi T, Shigyo T, Sugihara K, Takashio M, Emi S. J Biochem. 1996; 119:80–84. [PubMed: 8907179]
13. Kahn K, Serfozo P, Tipton PA. J Am Chem Soc. 1997; 119:5435–5442.
14. Ramazzina I, Folli C, Secchi A, Berni R, Percudani R. Nat Chem Biol. 2006; 2:144–148. [PubMed: 16462750]
15. Hernandez-Ortega A, Quesne MG, Bui S, Heyes DJ, Steiner RA, Scrutton NS, de Visser SP. J Am Chem Soc. 2015; 137:7474–7487. [PubMed: 25988744]
16. Fetzner S, Steiner RA. Appl Microbiol Biotechnol. 2010; 86:791–804. [PubMed: 20157809]
17. (a) Zhang YK, Liu HY, Yang WT. J Chem Phys. 2000; 112:3483–3492.(b) Zhang YK. J Chem Phys. 2005; 122:024114. [PubMed: 15638579] (c) Hu P, Zhang Y. J Am Chem Soc. 2006; 128:1272–1278. [PubMed: 16433545] (d) Zhang YK. Theor Chem Acc. 2006; 116:43–50.
18. (a) Li DM, Huang XQ, Han KL, Zhan CG. J Am Chem Soc. 2011; 133:7416–7427. [PubMed: 21513309] (b) Liu JJ, Zhang YK, Zhan CG. J Phys Chem B. 2009; 113:16226–16236. [PubMed: 19924840] (c) Zhang Y, Kua J, McCammon JA. J Am Chem Soc. 2002; 124:10572–10577. [PubMed: 12197759] (d) Zheng F, Yang WC, Ko MC, Liu JJ, Cho H, Gao DQ, Tong M, Tai HH, Woods JH, Zhan CG. J Am Chem Soc. 2008; 130:12148–12155. [PubMed: 18710224] (e) Liu JJ, Hamza A, Zhan CG. J Am Chem Soc. 2009; 131:11964–11975. [PubMed: 19642701] (f) Chen X, Fang L, Liu JJ, Zhan CG. J Phys Chem B. 2011; 115:1315–1322. [PubMed: 21175195] (g) Liu JJ, Zhao XY, Yang WC, Zhan CG. J Phys Chem B. 2011; 115:5017–5025. [PubMed: 21486046]
19. Frisch, MJ., Trucks, GW., Schlegel, HB., Scuseria, GE., Robb, MA., Cheeseman, JR., Montgomery, JA., Jr, Vreven, T., Kudin, KN., Burant, JC., Millam, JM., Iyengar, SS., Tomasi, J., Barone, V., Mennucci, B., Cossi, M., Scalmani, G., Rega, N., Petersson, GA., Nakatsuji, H., Hada, M., Ehara, M., Toyota, K., Fukuda, R., Hasegawa, J., Ishida, M., Nakajima, T., Honda, Y., Kitao, O., Nakai, H., Klene, M., Li, X., Knox, JE., Hratchian, HP., Cross, JB., Bakken, V., Adamo, C., Jaramillo, J., Gomperts, R., Stratmann, RE., Yazyev, O., Austin, AJ., Cammi, R., Pomelli, C., Ochterski, JW., Ayala, PY., Morokuma, K., Voth, GA., Salvador, P., Dannenberg, JJ., Zakrzewski, VG., Dapprich, S., Daniels, AD., Strain, MC., Farkas, O., Malick, DK., Rabuck, AD., Raghavachari, K., Foresman, JB., Ortiz, JV., Cui, Q., Baboul, AG., Clifford, S., Cioslowski, J., Stefanov, BB., Liu, G., Liashenko, A., Piskorz, P., Komaromi, I., Martin, RL., Fox, DJ., Keith, T., Al-Laham, MA., Peng, CY., Nanayakkara, A., Challacombe, M., Gill, PMW., Johnson, B., Chen, W., Wong, MW., Gonzalez, C., Pople, JA. Gaussian 03, Version C.02. Gaussian, Inc; Wallingford, CT: 2004.
20. Case, DA., Darden, TA., Cheatham, TE., Simmerling, CL., Wang, J., Duke, RE., Luo, R., Merz, KM., Wang, B., Pearlman, DA., Crowley, M., Brozell, S., Tsui, V., Gohlke, H., Mongan, J., Hornak, V., Cui, G., Beroza, P., Schafmeister, C., Caldwell, JW., Ross, WS., Kollman, PA. AMBER11. University of California; San Francisco: 2010.
21. Duan Y, Wu C, Chowdhury S, Lee MC, Xiong GM, Zhang W, Yang R, Cieplak P, Luo R, Lee T, Caldwell J, Wang JM, Kollman P. J Comput Chem. 2003; 24:1999–2012. [PubMed: 14531054]

22. Jorgensen WL, Chandrasekhar J, Madura JD, Impey RW, Klein ML. J Chem Phys. 1983; 79:926–935.

23. Case, DA., Darden, TA., Cheatham, TE., Simmerling, CL., Wang, J., Duke, RE., Luo, R., Merz, KM., Wang, B., Pearlman, DA., Crowley, M., Brozell, S., Tsui, V., Gohlke, H., Mongan, J., Hornak, V., Cui, G., Beroza, P., Schafmeister, C., Caldwell, JW., Ross, WS., Kollman, PA. AMBER8. University of California; San Francisco: 2004.

24. (a) Chen X, Fang L, Liu JJ, Zhan CG. Biochemistry. 2012; 51:1297–1305. [PubMed: 22304234] (b) Wei DH, Lei BL, Tang MS, Zhan CG. J Am Chem Soc. 2012; 134:10436–10450. [PubMed: 22697787] (c) Yao Y, Liu JJ, Zhan CG. Biochemistry. 2012; 51:8980–8992. [PubMed: 23092211] (d) Li DM, Huang XQ, Lin JP, Zhan CG. Dalton Trans. 2013; 42:3812–3820. [PubMed: 23303461] (e) Qiao Y, Han KL, Zhan CG. Biochemistry. 2013; 52:6467–6479. [PubMed: 23992153] (f) Wei DH, Fang L, Tang MS, Zhan CG. J Phys Chem B. 2013; 117:13418–13434. [PubMed: 24111489] (g) Wei DH, Huang XQ, Liu JJ, Tang MS, Zhan CG. Biochemistry. 2013; 52:5145–5154. [PubMed: 23862626] (h) Yao M, Tu WL, Chen X, Zhan CG. Org Biomol Chem. 2013; 11:7595–7605. [PubMed: 24097048] (i) Wei DH, Tang MS, Zhan CG. Org Biomol Chem. 2015; 13:6857–6865. [PubMed: 26018983]

25. (a) Feng J, Wang L, Liu H, Yang X, Liu L, Xie Y, Liu M, Zhao Y, Li X, Wang D, Zhan CG, Liao F. Appl Microbiol Biotechnol. 2015; 99:7973–7986. [PubMed: 25786739] (b) Feng T, Yang X, Wang D, Hu X, Liao J, Pu J, Zhao X, Zhan CG, Liao F. Appl Microbiol Biotechnol. 2017; 181:667–681.

26. Busi E, Sinicropi A, Terzuoli I, Marinello E, Basosi R. Appl Magn Reson. 2007; 31:471–482.

27. Altarsha M, Monard G, Castro B. Int J Quantum Chem. 2007; 107:172–181.

28. Simic MG, Jovanovic SV. J Am Chem Soc. 1989; 111:5778–5782.

29. Doll C, Bell AF, Power N, Tonge PJ, Tipton PA. Biochemistry. 2005; 44:11440–11446. [PubMed: 16114880]

30. (a) Eyring H. J Chem Phys. 1935; 3:107–115.(b) Truhlar DG, Garrett BC, Klippenstein SJ. J Phys Chem. 1996; 100:12771–12800.

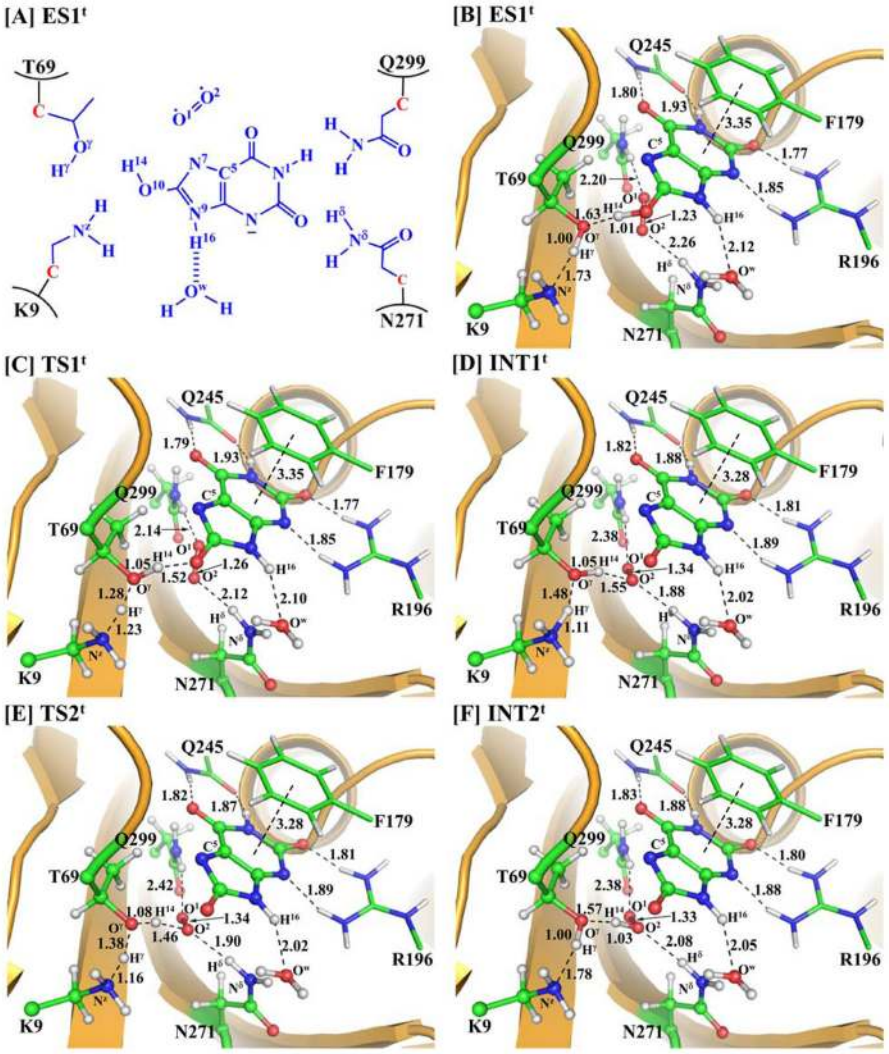

Figure 1.

(A) Division of the QM/MM system for uricase-catalyzed oxidation of 8-HX. Atoms in blue color were treated by the QM method. The boundary carbon atoms colored in red were treated with the improved pseudobond parameters. All other atoms were included in the MM subsystem. (B–F) Key configurations on the reaction pathway for uricase-catalyzed oxidation of 8-HX. The geometries were optimized at the QM/MM(B3LYP/6-31G*:AMBER) level. The key distances in the figure are in Å. Carbon, oxygen, nitrogen, and hydrogen atoms are colored in green, red, blue, and white, respectively. The backbone of the protein is rendered as ribbon and colored orange. The QM atoms are represented as balls and sticks and the surrounding residues are rendered as sticks or lines.

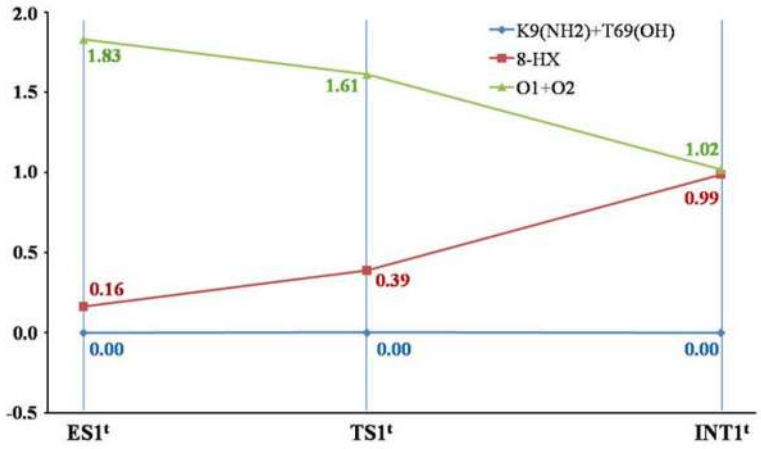

Figure 2.

The spin densities (SD) of the substrate 8-HX, oxygen, the groups K9-NH_2 and T69-OH in the key states along the reaction coordinate of reaction step 1 at the oxidation stage of uricase-catalyzed reaction.

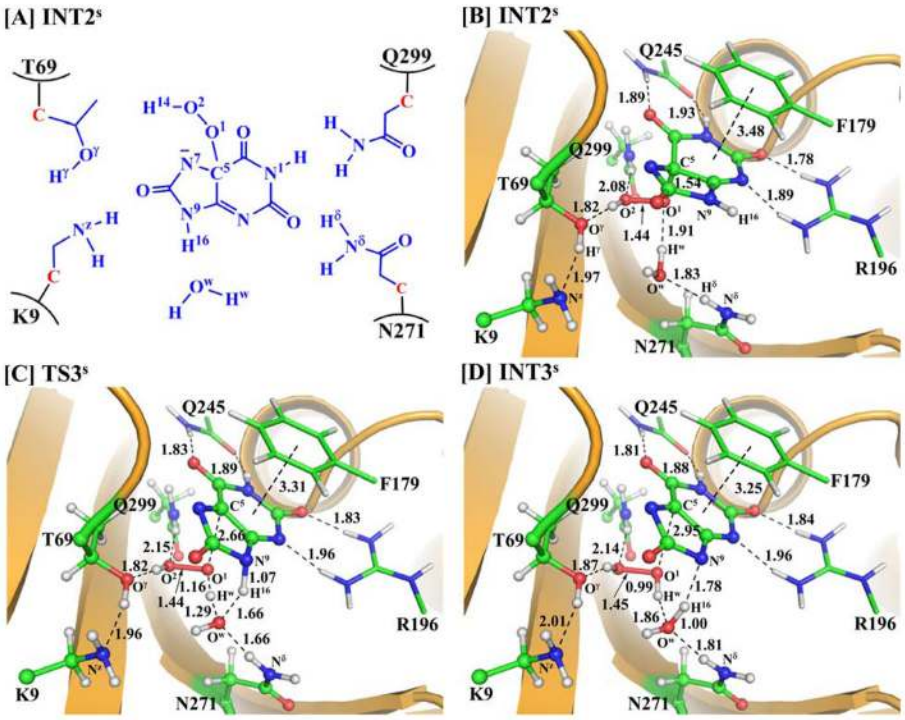

Figure 3.

(A) Division of the QM/MM system for reaction steps 3 and 4 along the uricase-catalyzed oxidation of 8-HX. Atoms in blue color were treated by the QM method. (B–D) Key configurations on the reaction pathway for the reaction steps 3 and 4 of the oxidation stage. The geometries were optimized at QM/MM(B3LYP/6-31G*:AMBER) level. The color scheme and division of the QM/MM system are similar to those in Figure 1.

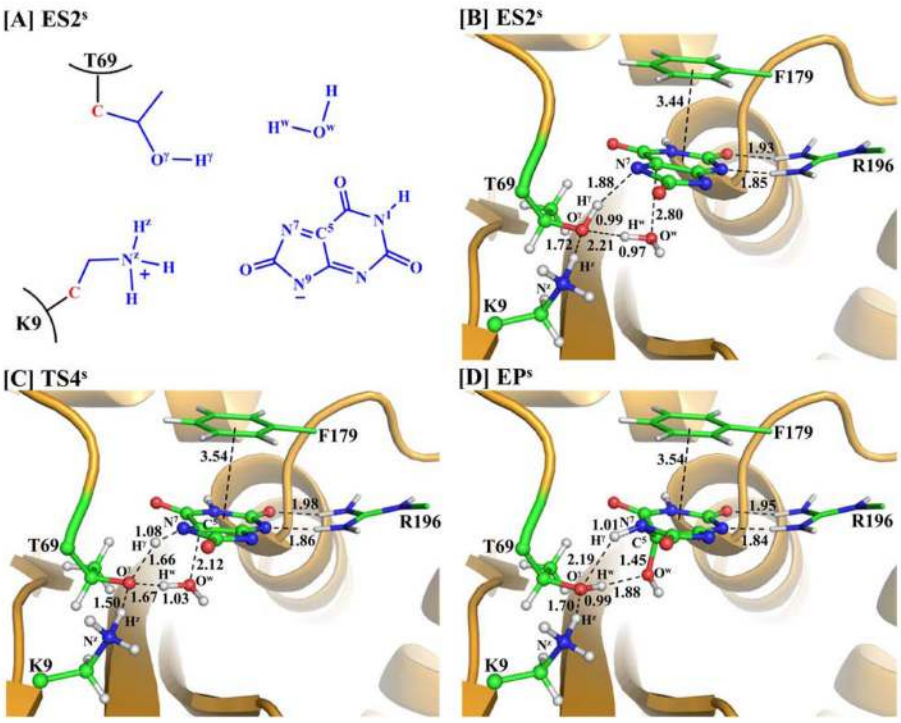

Figure 4.

(A) Division of the QM/MM system for the uricase-catalyzed hydration pathway *via* transition state TS4ˢ. Atoms in blue color were treated by the QM method. The boundary carbon atoms colored red were treated with the improved pseudobond parameters. All other atoms were included in the MM subsystem. (B–D) Key configurations on the reaction pathway *via* transition state TS4ˢ for the hydration stage. The geometries were optimized at QM/MM(B3LYP/6-31G*:AMBER) level. The color scheme is the same as that of Figure 1.

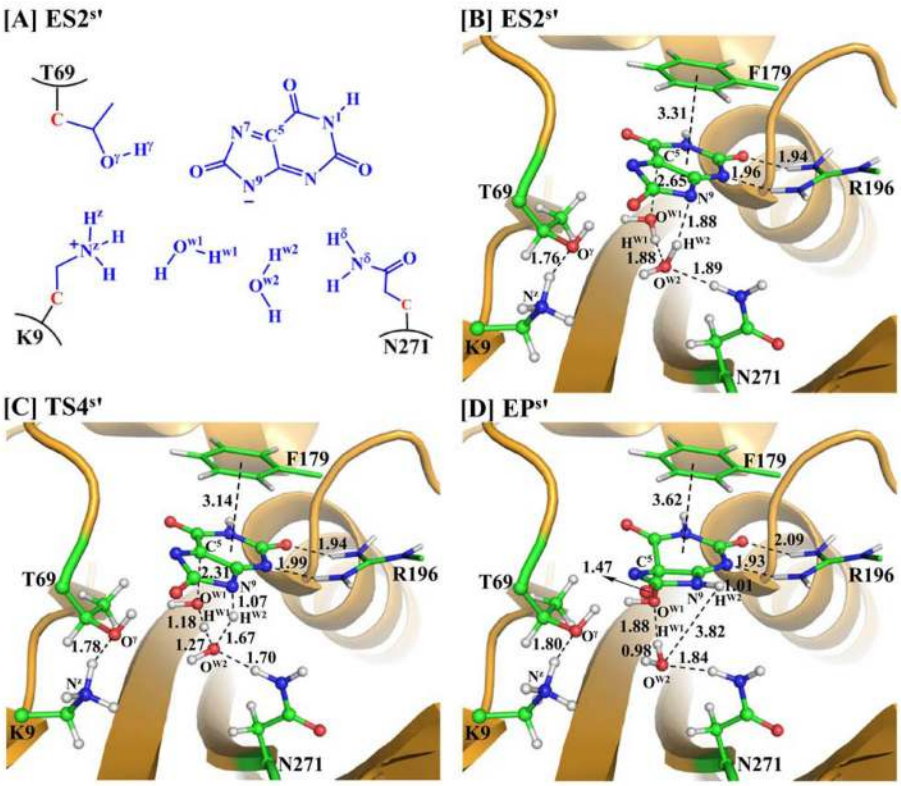

Figure 5.

(A) Division of the QM/MM system for the uricase-catalyzed hydration pathway *via* transition state TS4$^{s'}$. Atoms in blue color were treated by the QM method. The boundary carbon atoms colored red were treated with the improved pseudobond parameters. All other atoms were included in the MM subsystem. (B–D) Key configurations on the reaction pathway *via* transition state TS4$^{s'}$ for the hydration stage. The geometries were optimized at QM/MM(B3LYP/6-31G*:AMBER) level. The color scheme is the same as that of Figure 1.

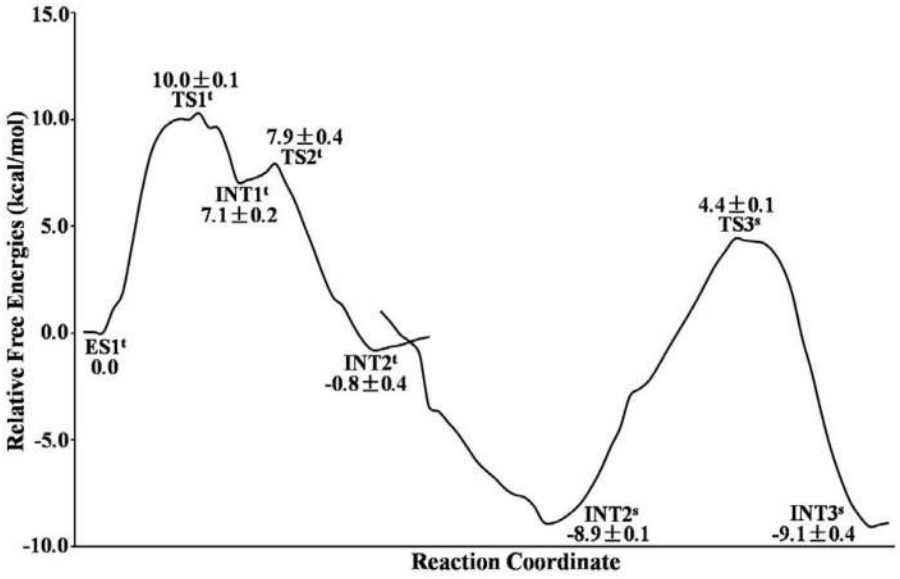

Figure 6.

Free energy profile for uricase-catalyzed oxidation of 8-HX. The relative free energies were determined with zero-point and thermal corrections for the QM subsystem. The QM/MM-FE calculations were performed at the B3LYP/6-31+G*:AMBER level for each QM/MM-optimized geometry along the reaction path.

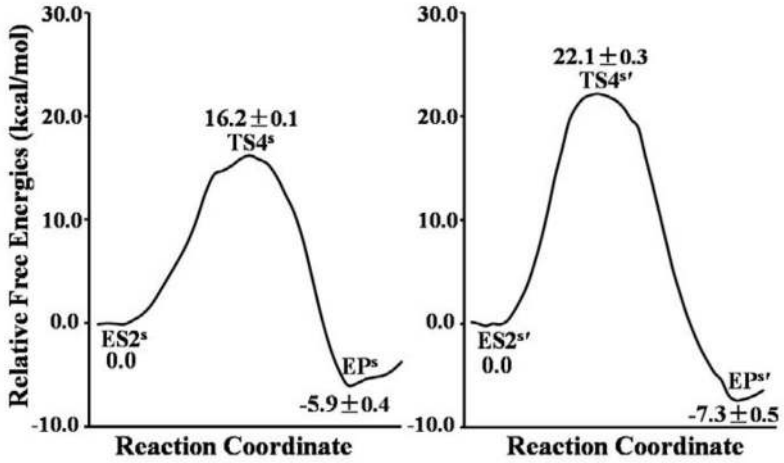

Figure 7.

Free energy profiles for uricase-catalyzed hydration associated with the two possible pathways. The relative free energies were determined with zero-point and thermal corrections for the QM subsystem. The QM/MM-FE calculations were performed at the B3LYP/6-31+G*:AMBER level for each QM/MM optimized geometry along the reaction path.

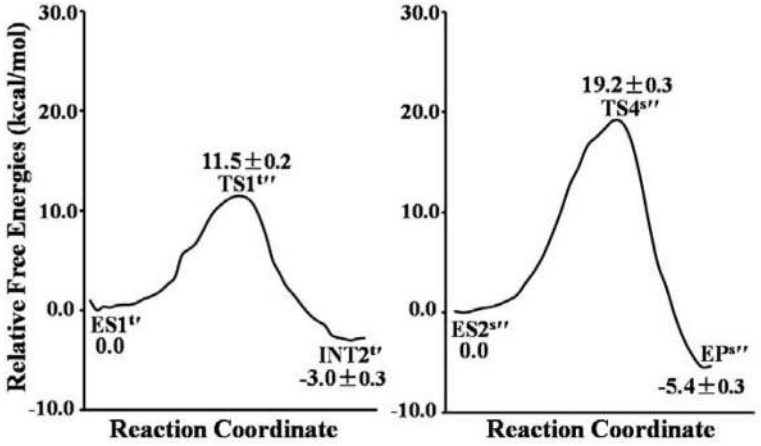

Figure 8.

Free energy profile for the possible alternative pathways depicted in Scheme 4. The relative free energies were determined with the zero-point and thermal corrections for the QM subsystem. The QM/MM-FE calculations were performed at the B3LYP/6-31+G*:AMBER level for each QM/MM-optimized geometry along the reaction path.

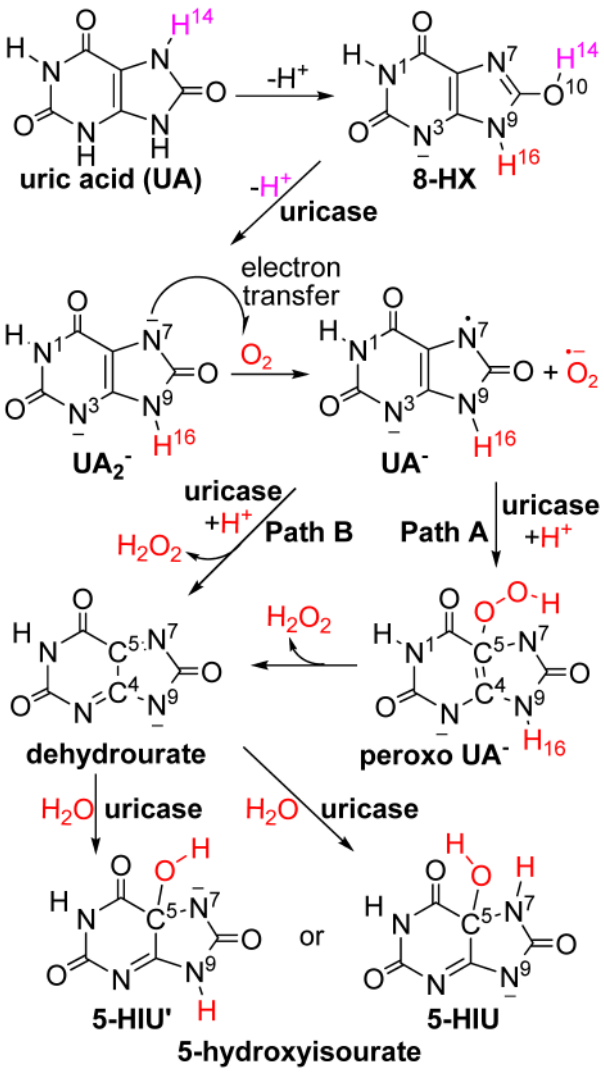

Scheme 1.

Proposed anion (−*e*, negatively charged) species 8-HX of UA, UA dianion (UA^{2-}), intermediate dehydrourate, and the products 5-hydroxyisourate that may exist in the uricase-catalyzed reaction process.

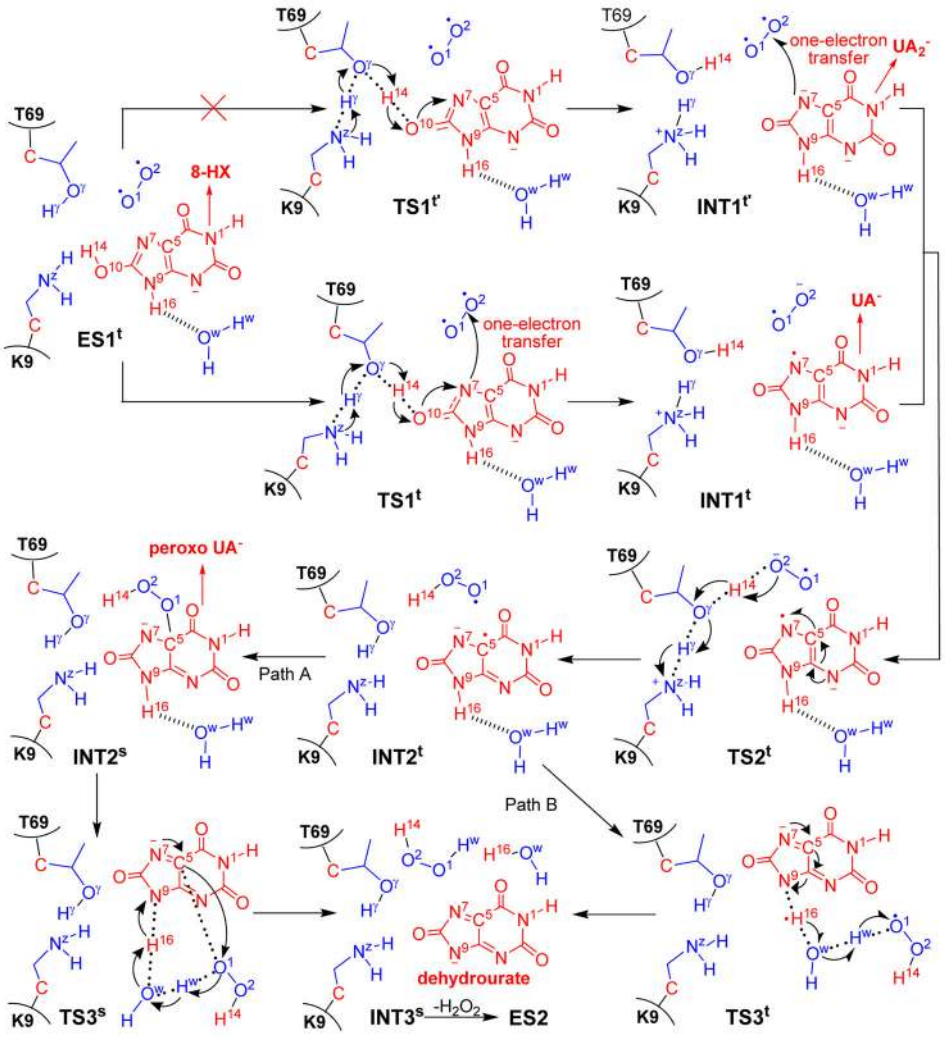

Scheme 2.

Proposed reaction pathways for the 8-HX oxidation stage of the uricase-catalyzed reaction of UA. The superscript "t" represents triplet, and the superscript "s" represents singlet.

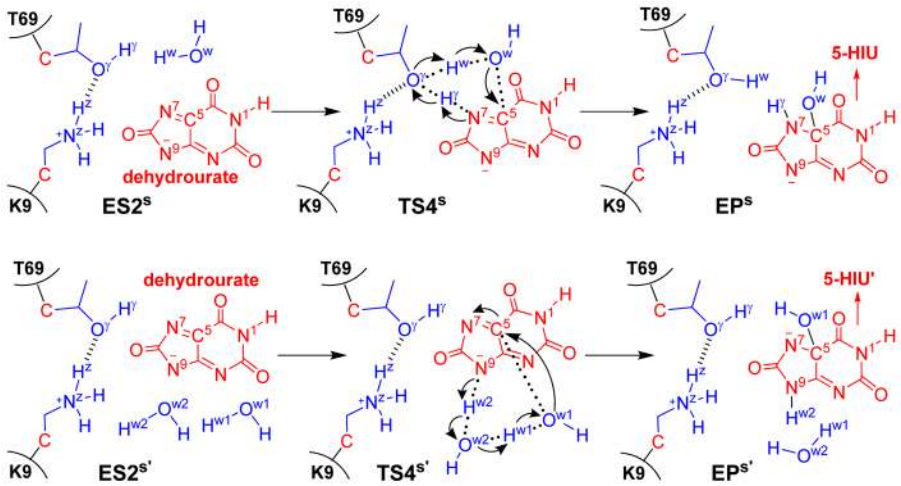

Scheme 3.

Proposed reaction pathways for the hydration stage of the uricase-catalyzed reaction of UA.

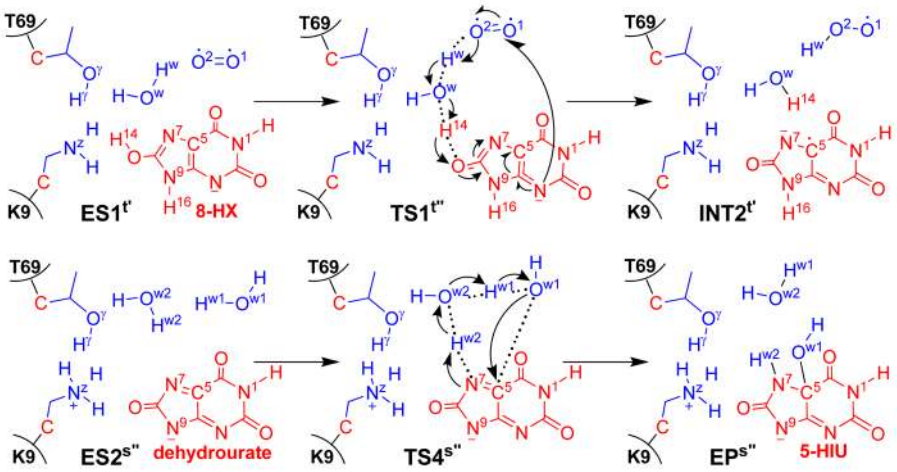

Scheme 4.

Other possible pathways that do not involve the residues Lys9 and Thr69 in the chemical reaction process.